Exceptional rigidity and biomechanics of amyloid revealed by 4D electron microscopy

Anthony W. P. Fitzpatrick, Sang Tae Park, and Ahmed H. Zewail[1]

Physical Biology Center for Ultrafast Science and Technology, Arthur Amos Noyes Laboratory of Chemical Physics, California Institute of Technology, Pasadena, CA 91125

Contributed by Ahmed H. Zewail, May 23, 2013 (sent for review April 4, 2013)

Amyloid is an important class of proteinaceous material because of its close association with protein misfolding disorders such as Alzheimer's disease and type II diabetes. Although the degree of stiffness of amyloid is critical to the understanding of its pathological and biological functions, current estimates of the rigidity of these β-sheet–rich protein aggregates range from soft (10^8 Pa) to hard (10^{10} Pa) depending on the method used. Here, we use time-resolved 4D EM to directly and noninvasively measure the oscillatory dynamics of freestanding, self-supporting amyloid beams and their rigidity. The dynamics of a single structure, not an ensemble, were visualized in space and time by imaging in the microscope an amyloid–dye cocrystal that, upon excitation, converts light into mechanical work. From the oscillatory motion, together with tomographic reconstructions of three studied amyloid beams, we determined the Young modulus of these highly ordered, hydrogen-bonded β-sheet structures. We find that amyloid materials are very stiff (10^9 Pa). The potential biological relevance of the deposition of such a highly rigid biomaterial in vivo are discussed.

cross-β structure | nanomechanics | microcantilever

Amyloid fibrils are filamentous polypeptide aggregates whose intra- and extracellular deposition is associated with more than 50 human disorders ranging from Alzheimer's disease to type II diabetes (1, 2). Normally soluble peptides or proteins with a wide range of amino acid sequences can aggregate into amyloid fibrils with a characteristic "cross-β" core structure composed of arrays of β-sheets running parallel to the long axis of the fibrils (3, 4). It is thought that this universal cross-β structure is responsible for the persistence and stability of these obdurate aggregates as a result of the long-range order of its hydrogen-bonded β-sheets (5–7). However, indirect ensemble measurements of the stiffness, or Young modulus (Y), of amyloid by statistical analysis of fluctuations in fibril shape have resulted in conflicting results, ranging from highly flexible [Y range of 90–320 MPa (8)] to extremely stiff [Y range of 2–14 GPa (6)]. More direct methods such as atomic force microscopy (AFM) nanoindentation, in which an AFM tip directly presses on an individual fibril to measure the contact stiffness, display an equally large Y range; results vary, e.g., for insulin fibrils, from 5 to 50 MPa (9) in one study and from 3 to 4 GPa (10) in another study.

The difference in Y of more than three orders of magnitude presents a serious question: is amyloid highly flexible like elastin [$Y = 1.1$ MPa (11)] or is it rigid like spider dragline silk [Y range of 1–10 GPa (12)]? To answer this important question, we measured Y values of amyloid "single particles" directly by visualizing in space and time the oscillations of three individual "amyloid beams" composed of the universal cross-β structure by using time-resolved 4D EM (13, 14).

Results and Discussion

Time-Resolved Dynamics of the Cross-β Steric Zipper. The concept is as follows: the high (spatiotemporal) resolution of 4D EM was used to visualize the biomechanics of amyloid beams (Fig. 1). Two separate, precisely timed electron and laser pulses were generated to (*i*) deliver at the beam a train of (probe) electron packets for imaging, or diffraction; and (*ii*) to heat or excite the amyloid beam; these are the initiating pulses at the specimen, thus defining the zero of time (pump pulse). By adjusting the time delay between the initiating pump pulse and the probing electron pulse, an image or "frame" is obtained. Structural dynamics over ranges of time scales (from femtoseconds to seconds) can be imaged with high spatiotemporal resolution (13). In this study, the spatial scale is in nanometers and the time scale is nanoseconds, as the oscillations of the beam can be observed on these scales.

We determine the stiffness of amyloid by using the pump laser beam to exert a tunable and highly accurate force on the amyloid beam, which represents a cantilever (15, 16), composed of paired hydrogen-bonded β-sheets (i.e., cross-β structure) (17). This driving force initiates the oscillations in the amyloid cantilever, like a diver induces damped vibrations in a diving board, and the resulting nanoscale displacements are imaged by using the probe pulse of electrons (Fig. 1). By precisely measuring the characteristic frequency of these oscillations from Fourier transforms, and by reconstructing the 3D shape of the three cantilevers from a set of images taken at different viewing angles (electron tomography; Fig. 2), the Y of amyloid was obtained (Fig. 3). Unlike in cantilevers of known shape, here we performed finite element analysis of these freestanding beams to accurately take into account the actual beam shape. Moreover, it was established that the amyloid beam over our range of impulsive excitation is elastic, i.e., below the irreversible plasticity range, from measurements of the displacement for a range of fluences (Fig. 4*B*).

The Amyloid Crystal Beam. Cocrystallization of the VQIVYK segment of tau protein with the dye Orange G results in bright orange crystals (17). The structure of the amyloid-like cocrystal has been solved by X-ray diffraction (17) (Figs. 1 and 5*A*). It contains ∼10% dye molecules situated within the void between the paired, cross–β-sheet structure (Figs. 1 and 5*B*); it also contains 36% water content, making these hydrated proteins (17). The intercalation of the dye molecules does not interfere with the packing within the cross-β structure (Figs. 1 and 5*B*), and therefore serves as a means to excite the amyloid-like crystal upon illumination by the visible light ($\lambda = 532$ nm). Individual crystals are needle-like (Fig. 2) as a result of hydrogen-bonded addition of VQIVYK molecules to the growing β-sheets along the long axis of the crystal (18). In our microscope, these crystals exhibit a strong electron diffraction pattern (Fig. 4*A*). The cocrystals are attached to the microscope grid in free space with nothing beneath them (Figs. 1 and 2). Observing the damped oscillations of a single beam indicates that the dye molecules indeed are the centers that induce the motion at time 0. We note that the bending (i.e., cantilever) motion here is induced because

Author contributions: A.W.P.F., S.T.P., and A.H.Z. designed research, performed research, contributed new reagents/analytic tools, analyzed data, and wrote the paper.

[1]To whom correspondence should be addressed. E-mail: zewail@caltech.edu.

This article contains supporting information online at www.pnas.org/lookup/suppl/doi:10.1073/pnas.1309690110/-/DCSupplemental.

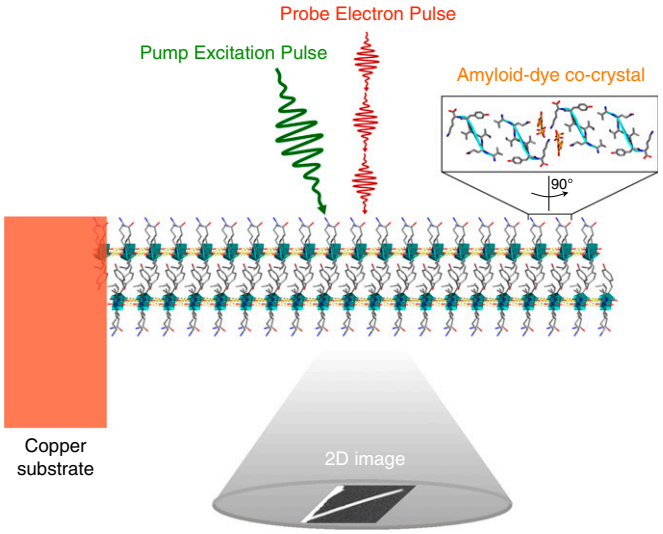

Fig. 1. 4D EM image of amyloid beams. Amyloid cantilevers are attached to a copper grid and excited by a pulsed green laser. The absorbing center is the Orange G dye molecule (orange) intercalated between a pair of steric zippers in the amyloid–dye cocrystal (*Inset*). The incorporation of this dye does not disrupt the cross-β structure, although it may stabilize adjacent steric zippers within the microcrystals. The photo-induced displacements are imaged by using timed electron packets and plotted.

light attenuates (Beer law) as it penetrates the crystal, causing more expansion of the face at which the light enters (19).

Amyloid Beam Tomography. Before examining the dynamics of the three amyloid beams, it was important to reconstruct the shape of the beams and how they were connected to the copper grid. This information is crucial, as the *Y* of a beam is a function of its size, shape, and frequency of oscillation (20). By incrementally rotating the sample stage and acquiring many different 2D views of the microcrystals, we were able to reconstruct the 3D shape of the amyloid beams by using electron tomographic methods. Fig. 2 depicts a comparison between representative 2D images of the cantilevers (Fig. 2, *Left*), tomographic 3D reconstructions (Fig. 2, *Middle*), and 2D back-projections of the cantilever reconstructions (Fig. 2, *Right*). The match between the 2D back-projections (Fig. 2, *Right*) and the original images (Fig. 2, *Left*) is very good, indicating that the 3D reconstruction is an accurate representation of the amyloid beams and that their "clamped" position to the copper grid (Fig. 2, *Middle*) justifies the cantilever description.

Dynamics of Amyloid Beams. Having defined the shapes of the three distinct amyloid beams, we then recorded the images and the evolution of beam image with time. It is important to note that the dynamics were obtained for a "single beam" and not for an ensemble of beams, which would provide an average; this may be the cause of the dispersion of literature results (6, 8–10). The space–time evolution of each beam is revealed by a time series of referenced difference images of the oscillating beams, in particular the motion of the beam tips (Fig. 3 *A*–*C* and Movies S1, S2, and S3). Images taken before the arrival of the heating pulse (at negative time) reveal no change, whereas those taken at positive times after time zero show clearly how the spatial position of the beam changes as a function of time delay (Fig. 3 *A*–*C* and Movies S1, S2, and S3). In all these imaging experiments, care was taken for any drift by always invoking a reference, here the copper grid.

The longitudinal and transverse displacements of the three amyloid beams are plotted in Fig. 3 *A*–*C*. They reveal the damped oscillatory motions with periods of the oscillation being 730 ns and 719 ns, respectively, for the first and second cantilevers, and this motion persists for many hundreds of cycles (>100 μs). The frequency of the oscillations, from the Fourier transform of the periodic displacements, are 1.37 MHz (Fig. 3*D*) and 1.39 MHz (Fig. 3*E*) for the first two beams. The motion of the third cantilever (Movie S3) displays two independent, orthogonal modes of oscillation. There are large longitudinal and transverse oscillations, and the plots of displacement (Fig. 3*C*) and the associated Fourier transforms (Fig. 3*F*) indicate that in the transverse and longitudinal directions, there are independent periodic motions with two distinct periods of 1,282 ns and 870 ns corresponding to frequencies of 0.78 MHz and 1.15 MHz, respectively. The observed oscillations do not arise from vibrations of the copper grid, as evident from the values of *Y* for these different amyloid beams. We also calculated the frequency for the grid and found it to be 22 MHz, significantly higher than that observed for the three amyloid beams studied.

The robustness of the fundamental flexural frequency, f_0, of each of the beams studied (Fig. 3 *D* and *F*), together with 3D reconstructions of their geometry from tomographic images (Fig. 2), enabled us to obtain *Y* for each beam. The density and Poisson ratio are 1.35 g/cm^3 (10) and 0.3 (21), respectively. Finite element analysis, which is necessary because of nonuniformity in cross-sections, was performed to obtain the lowest eigenfrequency that matches the experimentally observed frequency of oscillation. Furthermore, the displacements associated with the lowest eigenmode were mapped onto the 3D reconstructions (Fig. 3 *D*–*F*, *Inset*). The results for the first and second amyloid cantilever provide *Y* values of 1.0 GPa and 1.3 GPa, respectively. Because of the presence of two modes, analysis of the third cantilever results in a modulus in the range of 0.74 GPa

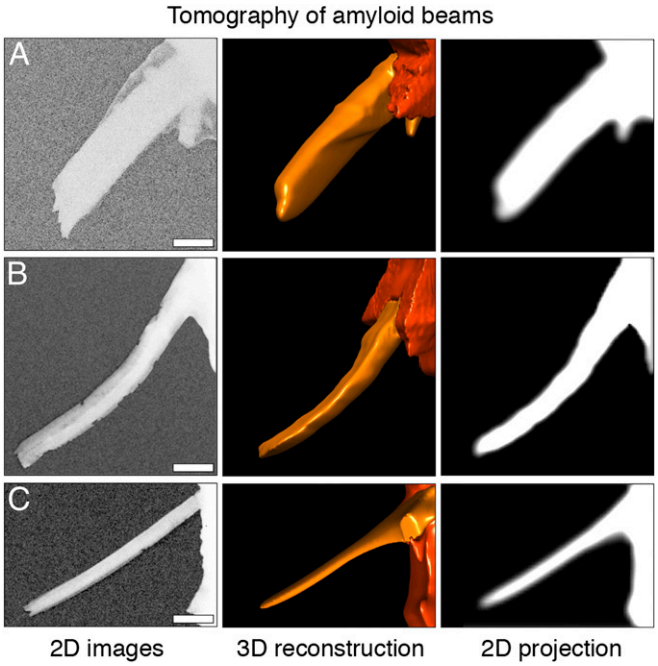

Fig. 2. Tomography of three amyloid single beams. (*A*–*C*) Representative images of the three different amyloid beams (*Left*) imaged by using the 4D time-resolved electron microscope; in the original images, electron density is shown in white. (Scale bar: 2 μm.) A series of images taken at different tilt angles was used to generate 3D reconstructions of the amyloid beams (*Middle*), where the protein density is shown in orange and the copper density is shown in red. To test the quality of these tomographic volumes, 2D back-projections of the 3D reconstructions were created (*Right*), they are in very good agreement with the original input images (*Left*).

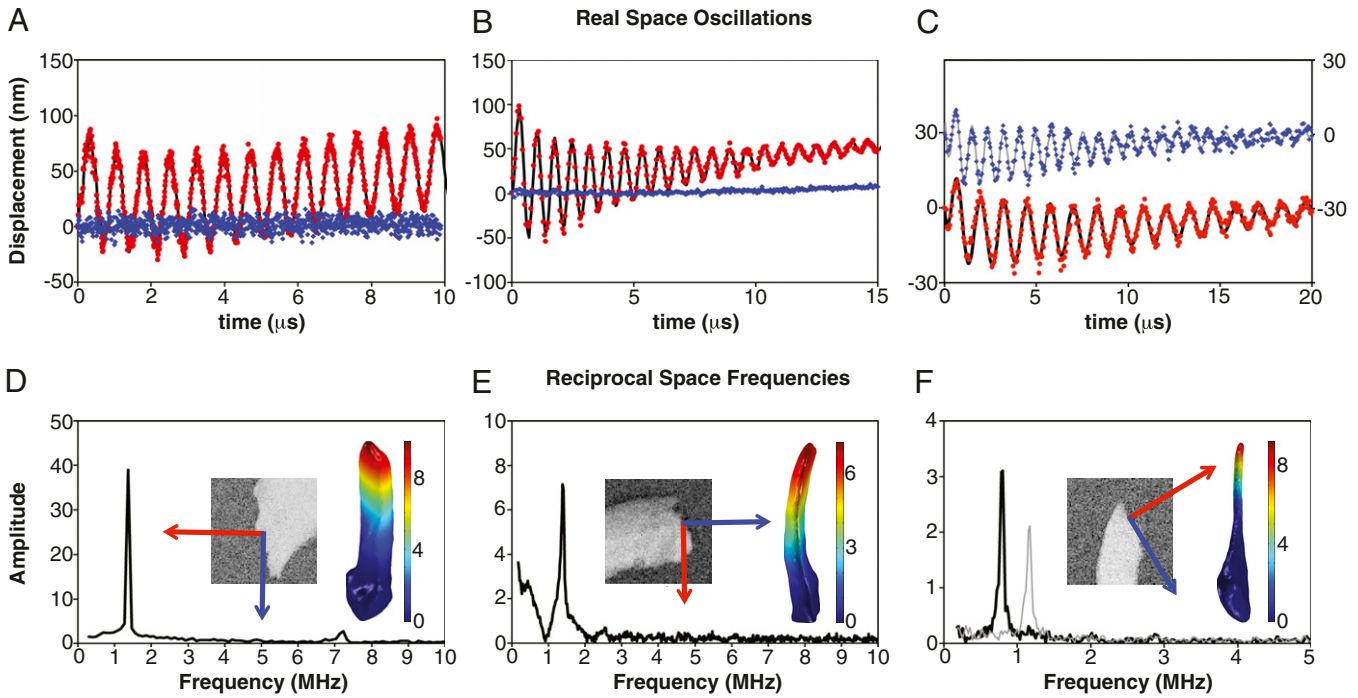

Fig. 3. Real-space, time-resolved oscillations of the amyloid beams. (*A–C*) Plotted major (red) and minor (blue) displacements of the amyloid cantilevers as a function of time. (*D–F*) Fourier transform of the periodic displacements giving the oscillation frequencies of the amyloid cantilevers. The directions of the major and minor oscillations of the tips of the amyloid cantilevers are shown (*Inset*). Finite element analysis was performed on the tomographic 3D reconstructions and used to match the simulated oscillation frequency to the experimentally observed frequency, thus determining *Y*. The displacements of the lowest eigenmode of each of the amyloid cantilevers are shown (*Inset*) in arbitrary units.

to 1.6 GPa, depending on whether the motion in the longitudinal or transverse direction (Fig. 3 *C* and *F*) corresponds to the dominant eigenmode, and this value too has an average of 1.17 GPa.

To confirm that all these measurements on three amyloid beams were made in the elastic regime, we measured the displacement as a function of laser fluence (Fig. 4*B*). The resulting stress (fluence)–strain (displacement) plot shows a linear behavior (correlation coefficient of 0.98). Furthermore, as the measured frequency remains constant, the *Y* value of amyloid is constant over the range of strains applied. The results of such experiments also highlight the reproducibility of the biomechanics of amyloid and demonstrate that radiation damage of the protein crystal is not of significance.

It is interesting to note that the mechanism of energy dissipation in amyloid materials can be determined from the damping of the observed oscillations (Fig. 3 *A–C*). Energy dissipation, or inverse quality factor $1/Q$, in the amyloid beams decreases linearly with increasing length (Fig. 4*C*), indicating

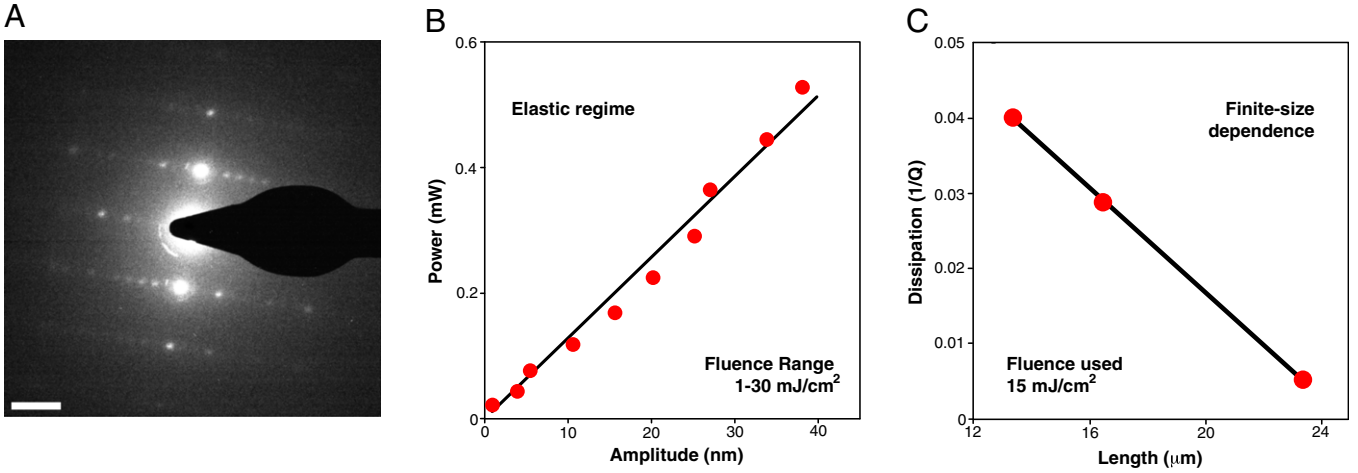

Fig. 4. Electron diffraction pattern, linear elasticity, and energy loss of amyloid beams. (*A*) A typical selected area diffraction pattern from an amyloid beam taken with our 4D electron microscope. (Scale bar: 2 nm^{-1}.) (*B*) The absence of irreversible plasticity was revealed by generating the stress (fluence)–strain (displacement) plot for the amyloid beam (Fig. 2*A*). Amplitude is defined as the SD of the longitudinal displacement. It is important to note that the oscillation frequency remained constant during the different measurements. (*C*) Plot of dissipation, inverse quality factor $1/Q$ vs. amyloid cantilever length (correlation coefficient = −0.99).

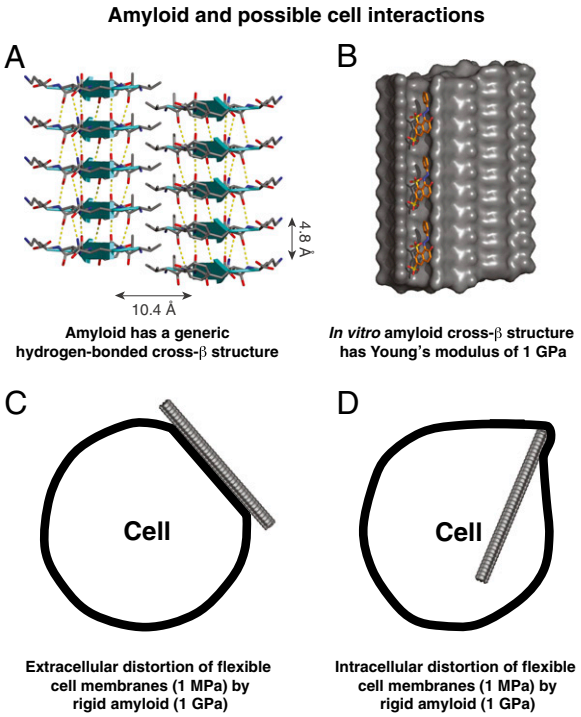

Fig. 5. Amyloid structure in vitro and a depiction of its likely interactions with biological cells (34, 35, 38). (*A*) The characteristic cross-β structure of amyloid (24) shown in atomic structure of VQIVYK amyloid-like microcrystals (17). The hydrogen-bonded 4.8-Å separation orthogonal to the 10.4-Å side-chain separation is a universal feature of amyloid materials (1). The β-sheet structure is shown as cyan ribbons with the peptide backbone depicted as sticks (carbon corresponds to gray, nitrogen corresponds blue, and oxygen corresponds to red) with hydrogen bonds shown as yellow dashes. (*B*) Cocrystallization of the VQIVYK segment of tau protein with the dye Orange G results in bright orange amyloid–dye microcrystals that are photoresponsive to green light. Note, however, that the dye molecule does not interfere with the cross-β structure and that the protein has 36% water content (17). (*C* and *D*) A possible model of how the rigidity of amyloid fibrils may influence the distortion (34, 35) or perforation of cell membranes (38) intra- and extracellularly.

a finite-size dependence (22, 23). The decreasing linear relationship between dissipation and size strongly suggests that internal defects in the amyloid beams increase linearly with increasing surface-to-volume ratio and that energy is lost via surface loss mechanisms (22, 23). These (intrinsic) surface-related defect mechanisms could include dangling hydrogen bonds at the tip, or unsatisfied side-chain interactions along the sides, of the amyloid beams. We rule out extrinsic dissipation mechanisms, such as clamping loss or thermoelastic energy dissipation, as we calculate, by using standard formulae (22), that these effects do not limit Q for our structures.

Biological Relevance. Significantly, the reported results show that the universal cross-β structure characteristic of amyloid (24) (Fig. 5*A*) is exceptionally stiff ($Y \sim 1$ GPa; Fig. 5*B*). Our measurements are in excellent agreement with the results of previous research by Smith et al. (10) and Knowles et al. (6) that used "single fibril" AFM nanoindentation [$Y = 3.3 \pm 0.4$ GPa (10)] and an (ensemble) fluctuation analysis approach [$Y = 2$–14 GPa (6)]. In contrast to other studies, which place the stiffness of amyloid in the low megapascal range [$Y = 5$–50 MPa by AFM nanoindentation (9) and $Y = 90$–320 using ensemble methods (8)], we unambiguously determine Y of amyloid materials to be in the low gigapascal range (~1 GPa).

The direct, noninvasive, and highly accurate nanomechanical testing of single-particle amyloid beams afforded by 4D EM demonstrates the unique advantages of this exciting technique compared with other methods for probing biomaterials on the nanoscale. Unlike AFM nanoindentation, which requires knowledge of the size or shape of the AFM tip to interpret the measured data (25), here the pump excitation pulse gently and nondestructively (Fig. 4*B*) photoinduces vibrations of the amyloid cantilever with a characteristic frequency. The (timed) probe electron pulse can then be used to precisely determine the dominant eigenfrequency (Fig. 3), and the dimensions (Fig. 2), of the single-particle amyloid beam that can be used to directly calculate Y. This is significant as the principal source of error in the (ensemble) fluctuation analysis approach to nanomechanical characterization of biomaterials is possible interactions with the substrate or between individual structures (25). None of these complications are present in our experimental setup (Fig. 1), making 4D EM the ideal tool to further explore the role played by amino acid sequence in modulating the rigidity of amyloid (6).

The high Y value (~1 GPa) of the cross-β structure (Fig. 5*B*) places amyloid among the most rigid proteinaceous materials in nature (6, 25), with a stiffness comparable to that of dragline spider silk (1–10 GPa) (12) and collagen fibers (~1 GPa) (26). This is intriguing, as the cross-β structure of amyloid shares many similarities with the crystalline regions of spider silk (27) and the triple helix of collagen (28) in that each of these materials consists of a network of intermolecular hydrogen bonds (Fig. 5*A*). Theoretically, the predicted performance limit of such maximally hydrogen-bonded proteinaceous materials is in the Y range of 10 to 20 GPa (6, 29).

Whereas collagen and spider silk are used purely as functional protein scaffold materials outside the cell, extracellular deposition of amyloid in vivo can play a physiological or pathological role depending on context (25). Amyloid plays a structural role in forming, e.g., bacterial coatings (30), but its unyielding nature is thought to be responsible for the stiffening of normally elastic tissue such as cardiac ventricles or blood vessel walls, thus disrupting normal function (31). For example, cerebral amyloid angiopathy is known to be associated with microhemorrhages caused by the deposition of Aβ fibrils within cerebral vessel walls (32), and the uncontrolled growth of amyloid plaques around the heart results in myocardial stiffness (31).

This hypothesis is conceivable from a materials point of view: the integration of highly rigid amyloid material into healthy elastic tissue creates a composite material (33). By the "rule of mixtures," this composite material will have stiffness given by the volume-weighted average of Y values of the constituent materials. Given that cell membranes are highly flexible ($Y \sim 1$ MPa) (33) and that amyloid is found here to be exceptionally stiff ($Y \sim 1$ GPa), the extracellular deposition of intractable amyloid plaques is likely to stiffen normally elastic or contractile tissues (8, 31). In addition, it has recently been shown that amyloid fibrils distort cell membranes (34, 35), which may lead to leakage and ultimately cell death, and this may be a pathological consequence of the inflexibility of amyloid's cross-β structure (Fig. 5*C*).

The high rigidity of amyloid ($Y \sim 1$ GPa) also has implications for protein aggregation within the cell. Our measurements show that the cross-β structure of amyloid is as intrinsically rigid as functional intracellular biological filaments such as actin and microtubuli [$Y \sim 3$ GPa and 1 GPa, respectively (36)]. However, unlike aberrant aggregation of proteins into amyloid fibrils, self-assembly of intracellular filaments such as actin has evolved to be readily reversible and is highly regulated (37). The unregulated growth of rigid amyloid fibrils in the intracellular environment is likely to distort cell membranes (Fig. 5*D*).

Indeed, a recently proposed mechanism for the pathogenesis of Alzheimer's disease strongly suggests that the rigidity of amyloid may be a crucial factor in disrupting normal cellular function (38). Accumulation of Aβ peptide within intracellular vesicles

leads to the outgrowth of stiff fibrils that penetrate the vesicular membrane, which results in cell death (38). By determining the exceptionally high intrinsic rigidity of the universal cross-β structure characteristic of amyloid, we hope to elucidate the role stiffness plays in the functional and pathological behavior of β-sheet aggregates in living organisms.

Conclusions

Here we have shown by direct and noninvasive visualization that periodic oscillations, and their stress–strain changes in space and time, can provide the rigidity or stiffness of single-particle amyloid beams. The *Y* value of the amyloid studied was measured to be exceptionally high (*ca*.1 GPa) for a proteinaceous material in the three beams imaged. The cooperative hydrogen bonds in the dense and highly ordered networks (i.e., crystals) are responsible, at least in part, for the exceptional rigidity that exceeds by three orders of magnitudes that of biological membranes. This is significant because the deposition of such a highly rigid material in vivo is likely to stiffen normally elastic or contractile tissues or to distort cell membranes and disrupt their function. With these reported proof-of-principle findings, numerous studies can now be carried out on amyloid, and indeed many other biomaterials, composed of different amino acid sequences and structures.

Materials and Methods

Amyloid-Like Microcrystal Preparation. VQIVYK–Orange G cocrystals were prepared as described previously (17). Droplets containing the needle-like crystals were deposited onto bare copper grids (300 and 400 mesh) and allowed to dry. Upon drying, needles would occasionally adhere to the copper grid, thus forming an amyloid cantilever.

Four-Dimensional EM of Amyloid Beams. The experimental setup is shown schematically in Fig. 1 and has been described for other materials previously (15). Briefly, VQIVYK–Orange G cocrystals suspended from a copper grid are excited by a green pulsed laser ($\lambda = 532$ nm, repetition rate 1 kHz) and the photoinduced movement of the amyloid-like microcrystals is imaged by timed electron packets (120 kV, LaB_6 source). The resulting displacements are determined from the series of time-resolved images by using in-house software.

Tomography, Image Processing, and 3D Reconstruction of Amyloid Beams. The frames of the tilt series (i.e., tomography) were obtained at 1° increments ranging from −58° to +58°, with essentially equal displacement from the 0° position in the clockwise and counterclockwise rotational directions. Images were aligned by using the "fiducialless alignment" option in ETOMO [part of the IMOD package (39)], and 3D reconstructions were created from the set of aligned images by using tomoJ (40). The 3D reconstructions were masked by using SPIDER (41). The appropriate tightness of the 3D mask was determined by using an iterative procedure of back-calculating the 2D projection from the masked 3D volume (using SPIDER) and matching to the set of experimental images. The thresholded 3D volumes were visualized in Chimera (42).

Finite Element Analysis of Amyloid Beams. The 3D reconstructions of the amyloid beams were directly exported from Chimera into a commercially available software package (COMSOL), and simulations of the amyloid cantilever motion were performed by using the solid mechanics module. The "clamp" position of the three cantilevers was accurately determined from the tomographic 3D reconstructions, and this was characterized as the "fixed point" in the motion of a fixed-free beam simulation. The mesh for the finite element calculation was extremely fine, with the number of elements ranging between 3,000 and 7,500 and the element volume ratio of the order of 10^{-4}. The experimental oscillation frequency was assumed to be the lowest eigenfrequency. In the finite element analysis, *Y* of the amyloid material was varied such that the simulated frequency of oscillation matched the experimentally observed frequency.

ACKNOWLEDGMENTS. This manuscript was reviewed by three experts: D. Eisenberg, C.M. Dobson and T.P.J. Knowles. A.W.P.F. was previously a postdoctoral associate with C.M. Dobson who is a pioneer in the field of amyloid research. We are grateful to all reviewers for their helpful and penetrating comments. We thank H. B. Gristick for help with sample preparation and for useful discussions. This work was supported by National Science Foundation Grant DMR-0964886 and Air Force Office of Scientific Research Grant FA9550-11-1-0055 to the Gordon and Betty Moore Center for Physical Biology at the California Institute of Technology.

1. Chiti F, Dobson CM (2006) Protein misfolding, functional amyloid, and human disease. *Annu Rev Biochem* 75:333–366.
2. Dobson CM (2003) Protein folding and misfolding. *Nature* 426(6968):884–890.
3. Fitzpatrick AWP, et al. (2013) Atomic structure and hierarchical assembly of a cross-β amyloid fibril. *Proc Natl Acad Sci USA* 110(14):5468–5473.
4. Eisenberg D, Jucker M (2012) The amyloid state of proteins in human diseases. *Cell* 148(6):1188–1203.
5. Baldwin AJ, et al. (2011) Metastability of native proteins and the phenomenon of amyloid formation. *J Am Chem Soc* 133(36):14160–14163.
6. Knowles TPJ, et al. (2007) Role of intermolecular forces in defining material properties of protein nanofibrils. *Science* 318(5858):1900–1903.
7. Tsemekhman K, Goldschmidt L, Eisenberg D, Baker D (2007) Cooperative hydrogen bonding in amyloid formation. *Protein Sci* 16(4):761–764.
8. Sachse C, Grigorieff N, Fändrich M (2010) Nanoscale flexibility parameters of Alzheimer amyloid fibrils determined by electron cryo-microscopy. *Angew Chem Int Ed Engl* 49(7):1321–1323.
9. Guo SL, Akhremitchev BB (2006) Packing density and structural heterogeneity of insulin amyloid fibrils measured by AFM nanoindentation. *Biomacromolecules* 7(5): 1630–1636.
10. Smith JF, Knowles TPJ, Dobson CM, Macphee CE, Welland ME (2006) Characterization of the nanoscale properties of individual amyloid fibrils. *Proc Natl Acad Sci USA* 103(43): 15806–15811.
11. Aaron BB, Gosline JM (1981) Elastin as a random-network elastomer—a mechanical and optical analysis of single elastin fibers. *Biopolymers* 20(6):1247–1260.
12. Vollrath F, Knight DP (2001) Liquid crystalline spinning of spider silk. *Nature* 410 (6828):541–548.
13. Zewail AH (2010) Four-dimensional electron microscopy. *Science* 328(5975):187–193.
14. Zewail AH, Thomas JM (2010) *4D Electron Microscopy: Imaging in Time and Space* (Imperial College Press, London).
15. Flannigan DJ, Samartzis PC, Yurtsever A, Zewail AH (2009) Nanomechanical motions of cantilevers: Direct imaging in real space and time with 4D electron microscopy. *Nano Lett* 9(2):875–881.
16. Lorenz UJ, Zewail AH (2013) Biomechanics of DNA structures visualized by 4D electron microscopy. *Proc Natl Acad Sci USA* 110(8):2822–2827.
17. Landau M, et al. (2011) Towards a pharmacophore for amyloid. *PLoS Biol* 9(6): e1001080.
18. Nelson R, et al. (2005) Structure of the cross-beta spine of amyloid-like fibrils. *Nature* 435(7043):773–778.
19. Warner M, Mahadevan L (2004) Photoinduced deformations of beams, plates, and films. *Phys Rev Lett* 92(13):134302.
20. Meirovich L (1986) *Elements of Vibration Analysis.* (McGraw-Hill, New York).
21. Grellman W, Seidler S (2001) *Deformation and Fracture Behavior of Polymers* (Springer, Berlin).
22. Yasumura KY, et al. (2000) Quality factors in micron- and submicron-thick cantilevers. *J Microelectromech Syst* 9(1):117–125.
23. Mohanty P, et al. (2002) Intrinsic dissipation in high-frequency micromechanical resonators. *Phys Rev B* 66(8):085416.
24. Sunde M, et al. (1997) Common core structure of amyloid fibrils by synchrotron X-ray diffraction. *J Mol Biol* 273(3):729–739.
25. Knowles TPJ, Buehler MJ (2011) Nanomechanics of functional and pathological amyloid materials. *Nat Nanotechnol* 6(8):469–479.
26. Shen ZL, Dodge MR, Kahn H, Ballarini R, Eppell SJ (2008) Stress-strain experiments on individual collagen fibrils. *Biophys J* 95(8):3956–3963.
27. Slotta U, et al. (2007) Spider silk and amyloid fibrils: A structural comparison. *Macromol Biosci* 7(2):183–188.
28. Cowan PM, McGavin S, North ACT (1955) The polypeptide chain configuration of collagen. *Nature* 176(4492):1062–1064.
29. Keten S, Xu ZP, Ihle B, Buehler MJ (2010) Nanoconfinement controls stiffness, strength and mechanical toughness of beta-sheet crystals in silk. *Nat Mater* 9(4):359–367.
30. Chapman MR, et al. (2002) Role of Escherichia coli curli operons in directing amyloid fiber formation. *Science* 295(5556):851–855.
31. Pepys MB (2006) Amyloidosis. *Annu Rev Med* 57:223–241.
32. Fändrich M, Schmidt M, Grigorieff N (2011) Recent progress in understanding Alzheimer's β-amyloid structures. *Trends Biochem Sci* 36(6):338–345.
33. Lulevich V, Zimmer CC, Hong HS, Jin LW, Liu GY (2010) Single-cell mechanics provides a sensitive and quantitative means for probing amyloid-beta peptide and neuronal cell interactions. *Proc Natl Acad Sci USA* 107(31):13872–13877.
34. Engel MFM, et al. (2008) Membrane damage by human islet amyloid polypeptide through fibril growth at the membrane. *Proc Natl Acad Sci USA* 105(16): 6033–6038.
35. Milanesi L, et al. (2012) Direct three-dimensional visualization of membrane disruption by amyloid fibrils. *Proc Natl Acad Sci USA* 109(50):20455–20460.
36. Gittes F, Mickey B, Nettleton J, Howard J (1993) Flexural rigidity of microtubules and actin filaments measured from thermal fluctuations in shape. *J Cell Biol* 120(4): 923–934.

37. Pantaloni D, Hill TL, Carlier MF, Korn ED (1985) A model for actin polymerization and the kinetic effects of ATP hydrolysis. *Proc Natl Acad Sci USA* 82(21):7207–7211.
38. Friedrich RP, et al. (2010) Mechanism of amyloid plaque formation suggests an intracellular basis of Abeta pathogenicity. *Proc Natl Acad Sci USA* 107(5): 1942–1947.
39. Kremer JR, Mastronarde DN, McIntosh JR (1996) Computer visualization of three-dimensional image data using IMOD. *J Struct Biol* 116(1):71–76.
40. Messaoudii C, Boudier T, Sanchez Sorzano CO, Marco S (2007) TomoJ: Tomography software for three-dimensional reconstruction in transmission electron microscopy. *BMC Bioinformatics* 8:288.
41. Frank J, et al. (1996) SPIDER and WEB: Processing and visualization of images in 3D electron microscopy and related fields. *J Struct Biol* 116(1):190–199.
42. Pettersen EF, et al. (2004) UCSF Chimera—a visualization system for exploratory research and analysis. *J Comput Chem* 25(13):1605–1612.